

## RESEARCH ARTICLE

10.1002/2015JB012511

## Key Points:

- Infragravity energy is observed on horizontal components of two buried ocean bottom seismometers
- Correlations with local weather provide strong evidence for nearshore infragravity wave generation
- Infragravity wave directionality can be measured as a function of frequency

## Correspondence to:

A. K. Doran,  
adoran@ucsd.edu

## Citation:

Doran, A. K., and G. Laske (2016), Infragravity waves and horizontal seafloor compliance, *J. Geophys. Res. Solid Earth*, 121, 260–278, doi:10.1002/2015JB012511.

Received 9 SEP 2015

Accepted 14 DEC 2015

Accepted article online 16 DEC 2015

Published online 26 JAN 2016

## Infragravity waves and horizontal seafloor compliance

Adrian K. Doran<sup>1</sup> and Gabi Laske<sup>1</sup>
<sup>1</sup>Institute of Geophysics and Planetary Physics, University of California, San Diego, La Jolla, California, USA

**Abstract** We report the first consistent observation of horizontal seafloor compliance induced by infragravity (IG) waves. Long-period IG ocean waves manifest themselves as broad, dominant features in ocean bottom pressure and vertical deformation spectra, but signals are rarely (if ever) identified on the horizontal components of traditional ocean bottom seismometers (OBS) due to low signal level and high current-induced tilt noise at long periods. We examine two OBS stations with shallow-buried seismometers: the Monterey Ocean Bottom Broadband site offshore California and the Ocean Seismic Network (OSN) pilot site OSN1B near Hawaii. We use nearby weather buoys to investigate the relationship between the presence of infragravity waves and environmental conditions. We find strong evidence that infragravity wave generation is primarily confined to the near-coastal environment. Additional IG source information is found by examining the directionality of passing IG waves as a function of frequency, which we analyze using the coherence between pressure and the two horizontal components. Finally, we evaluate the implications for a joint vertical and horizontal compliance inversion.

## 1. Introduction

Energy from oceanic infragravity (IG) waves dominates the long-period power spectra of broadband ocean bottom seismometers. Infragravity waves in the deep ocean have small wave heights ( $\leq 1$  cm), long wavelengths (1–20 km), long periods (30–300 s), and high phase velocities ( $> 100$  m/s in 2 km water depth) and propagate great distances over the ocean while experiencing minimal attenuation [Yang *et al.*, 2012; Webb, 1998]. Observations were first made near the coast [Munk, 1949; Tucker, 1950] but infragravity energy is now routinely observed in the open ocean as well [Webb *et al.*, 1991; Godin *et al.*, 2013]. The mechanism of infragravity wave generation remains a target of intense study. Significant correlation has been reported between infragravity waves and local short-period wind and swell waves [e.g., Herbers *et al.*, 1995a; Ardhuin *et al.*, 2014]. Consensus is slowly building that infragravity waves are formed by nonlinear interactions of short-period ocean waves in the nearshore environment that either become trapped on the continental shelf or leak outward into the deep ocean [e.g., Herbers *et al.*, 1995b; Webb, 1998; Rhie and Romanowicz, 2006; Aucan and Ardhuin, 2013; Ardhuin *et al.*, 2014; Godin *et al.*, 2014; Crawford *et al.*, 2015].

Infragravity energy can be observed on broadband ocean bottom seismometers (OBSs) and pressure sensors in all regions of the ocean. Infragravity studies have a wide range of applications in both seismology and oceanography. Infragravity waves play a role in sediment transport and other nearshore processes [Dolenc *et al.*, 2005] and have been proposed as a source of the Earth's continuous free oscillations [Rhie and Romanowicz, 2006]. Recent work has suggested that long-period IG waves may transmit mechanical energy between the ocean and atmosphere [Godin and Fuks, 2012], and some investigators have linked open ocean IG waves with ice-shelf deformation [Bromirski *et al.*, 2010]. Seafloor compliance studies utilize the transfer function between the pressure and acceleration in the infragravity band to investigate crustal elastic structure [Crawford *et al.*, 1991, 1998; Willoughby *et al.*, 2008; Zha *et al.*, 2014]. In order to lower regional and teleseismic detection thresholds on OBSs, infragravity noise can be deconvolved from the time series using concurrent seafloor pressure records [Crawford *et al.*, 1999; Crawford and Webb, 2000; Taira *et al.*, 2014].

Current studies involving OBS focus on characterizing infragravity energy on vertical acceleration recordings. Low instrument self-noise on modern broadband instruments and high coherence between vertical acceleration and pressure over a broad range of frequencies allows easy association with infragravity waves. Infragravity energy and deformation occur in the horizontal plane as well as the vertical plane, but thus far high noise levels have inhibited their study [Crawford *et al.*, 1991; Crawford and Singh, 2008]. The noise is primarily caused by current-induced tilt, is significant particularly at long periods and at installations in shallow water, and can overwhelm even very strong teleseismic arrivals [Webb, 1998].

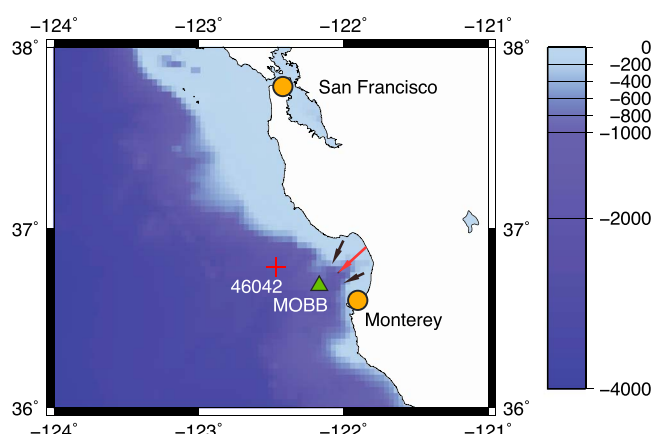


**Figure 1.** Location map for Monterey Ocean Bottom Broadband station (MOBB). The water depth at the OBS site is 1036 m. Also shown is the closest NOAA buoy (46042), 24 km northwest of MOBB. The arrows depict the primary inferred source azimuths of infragravity waves as described in section 5.3. The red arrow is the median azimuth.

Two factors obscure the horizontal infragravity signal on OBSs: the horizontal deformation due to vertical loading is inherently smaller in magnitude than the vertical deformation [e.g., *Iassonov and Crawford, 2008*] and tilt noise dominates the ambient spectrum of horizontal OBS components at long periods [e.g., *Webb, 1998; Duennebie and Sutton, 1995*]. Tilt noise is caused by seafloor currents flowing past an instrument and by the turbulence and eddies created by nonlinear interactions between the fluid and the package. The lower the profile of the instrument, the less long-period noise is induced, and burial of the instrument minimizes the effects of this noise [Duennebie and Sutton, 2007]. Buried OBSs allow us for the first time to characterize infragravity waves using horizontal components. We investigate 1 month long data segments at two such sites: the Monterey Ocean Bottom Broadband (MOBB) site offshore California [Romanowicz et al., 2006] (Figure 1) and the Ocean Seismic Network (OSN) pilot site OSN1B near Hawaii [Dziewonski et al., 1992a] (Figure 2). Buried seismometers can be between 20–50 dB quieter than seafloor instruments at long periods [Duennebie and Sutton, 1995; Collins et al., 2001], and studies of both OSN1B [Crawford and Webb, 2000] and MOBB [Dolenc et al., 2007] records confirm that tilt noise at these sites is negligible.

For OSN1, we concentrate our study on the buried package OSN1B [Collins et al., 2001]. Both MOBB and OSN1B are buried in the sediment such that the top of the package is at least 10 cm beneath the seafloor [Stephen et al., 2003; Romanowicz et al., 2006]. In this paper, we briefly introduce the IG terminology and detail our analysis method. For the 1 month long data segments, we examine the feasibility and measures required to optimize observed horizontal compliance. We study the relationship between horizontally recorded infragravity energy and local weather conditions, and try to infer whether IG waves are generated near the coast

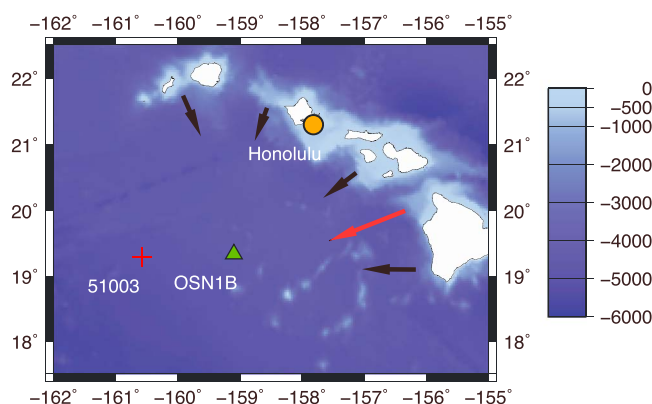


**Figure 2.** Location map for Ocean Seismic Network pilot station OSN1B near Hawaii. The water depth at the OBS site is 4150 m. Also shown is the closest NOAA buoy (51003), about 100 km west of OSN1B. The arrows depict the primary inferred source azimuths of infragravity waves as described in section 5.3. The red arrow is the median azimuth.

or in the deep ocean basin. We also examine the directionality of IG waves as revealed by the two orthogonal horizontal components at both OBS sites. Lastly, we discuss the potential of joint vertical and horizontal compliance studies to retrieve seismic anisotropy in marine sediments.

## 2. Theory and Terminology

Infragravity waves propagate through the oceans and create a pressure signal on the seafloor; this pressure then induces ground deformation (and consequently ground acceleration). The seafloor pressure at a water depth  $H$  caused by a surface gravity wave of height  $\zeta$  is given by

$$P_{\text{bottom}} = \frac{\rho g \zeta}{\cosh(kH)} \simeq P_{\text{surface}} e^{kH} \quad (1)$$

where  $k$  is the wave number,  $\rho$  is the water density, and  $g$  is the gravitational acceleration [e.g., Dolenc *et al.*, 2005]. Infragravity waves are freely propagating surface gravity waves [Webb *et al.*, 1991], and the frequency and wave number are related through the dispersion relation [Abel, 1987]

$$\omega^2 = gk \tanh(kH) \quad (2)$$

where  $\omega$  is the angular frequency of the wave. The ground deformation is a function of the underlying elastic structure. An analytic normalized compliance expression (the ratio of deformation to vertical stress, normalized by the wave number) can be derived for an elastic half-space [Crawford, 2004]:

$$\eta = k\xi = k \frac{\mathbf{u}}{\tau_{zz}} = k \frac{u_x \hat{x} + u_z \hat{z}}{\tau_{zz}} = \frac{-i}{2(\lambda + \mu)} \hat{x} + \frac{\lambda + 2\mu}{2\mu(\lambda + \mu)} \hat{z} \quad (3)$$

where  $\mathbf{u}$  is the displacement,  $\tau_{zz}$  is the vertical stress, and  $\lambda$  and  $\mu$  are the Lamé parameters. Displacement is expected in both the vertical and horizontal directions, but to date, no studies have focused on horizontal deformation.

The water depth controls the maximum frequency to which either horizontal or vertical coherence in the IG frequency band can be analyzed [Crawford *et al.*, 1991]. Depending on the wave height of the infragravity waves at the sea surface, the highest frequency that waves can have to exert pressure on the seafloor are those with wavelengths between 0.5 to 2 times the water depth. With the wave number,  $k$ , becoming

$$k = 2\pi/(nH), \quad 0.5 < n < 2 \quad (4)$$

using equation (2),  $\omega = 2\pi f$ , and with  $\tanh(2\pi/n) \simeq 1$ ,  $n \leq 2$ , this gives a maximum frequency for IG waves that exert significant pressure on the seafloor

$$f_c = \left[ \frac{g}{2\pi H n} \right]^{1/2}, \quad 0.5 < n < 2 \quad (5)$$

At OSN1B, the water depth is 4150 m, so the respective frequencies are 27 and 14 mHz (for  $n = 0.5; 2$ ). At MOBB, the water depth is 1036 m, so the respective frequencies are 55 and 27 mHz. In principle, we should then expect that IG waves at MOBB contain higher frequencies than at OSN. To keep the comparison simple, however, we low-pass filter the data from both sites at 30 mHz. Infragravity waves continue to periods of 1000 s and longer [Aucan and Ardhuin, 2013], but we are limited by the instrument response of the seismometers and differential pressure gauges (Figure 3). We therefore restrict our analysis to frequencies between 5 and 30 mHz.

We note that the instrument responses listed in the Incorporated Research Institutions for Seismology Data Management Center (IRIS DMC) metadata files for the OSN1B instruments (the pressure gauge and all seismometer components) were grossly inconsistent with our observations. Inquiries with OSN PIs Frank Vernon and John Collins revealed that these responses are, in fact, incorrect. We obtained the correct values from J. Collins (personal communication, 2015) and incorporate those into our analysis. Details of the instrument responses can be found in Appendix A.

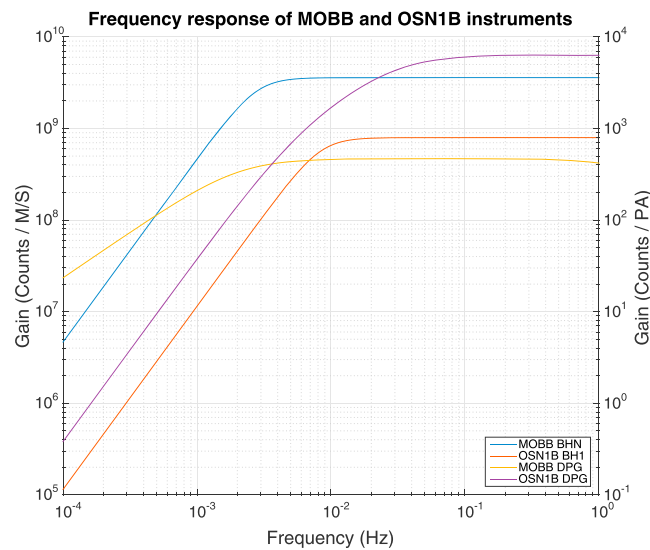


**Figure 3.** Instrument responses of the sensors used in this study. The seismometer at MOBB is a Guralp CMG-1T, while the seismometer at OSN1B is a Guralp CMG-3T. The pressure sensor at both MOBB and OSN1B is a Cox-Webb DPG. The responses for MOBB are available at the IRIS DMC; see Appendix A for details of the OSN1B responses.

### 3. Site Description

The 1998 Ocean Seismic Network Pilot Experiment (OSNPE) studied the feasibility of adding permanent oceanic seismic stations to the Global Seismic Network [Stephen *et al.*, 2003]. The site was 225 km southwest of the island of Oahu, where the seafloor is 4150 m below the sea surface. The OSNPE consisted of three instrument packages. OSN1 was a very broadband three-component Teledyne KS-54000 borehole seismometer and was installed approximately 240 m below the seafloor in Ocean Drilling Program (ODP) Hole 843B [Dziewonski *et al.*, 1992a]. Data for this sensor are available at the Incorporated Research Institutions for Seismology (IRIS) Data Management Center (DMC) between 3 February and 29 May. OSN1B was a package composed of a broadband three-component Guralp CMG-3T seismometer and a Cox-Webb differential pressure gauge (DPG) [Cox *et al.*, 1984]. It was installed one meter below the seafloor, and data are available at the IRIS DMC between 3 February and 14 June. OSN1S used identical equipment as OSN1B but was deployed directly on the seafloor. Its data are available between 7 February and 14 June. The long-period horizontal signal on the borehole instrument was degraded by fluid convection in the well, but analysis of OBS1B records showed that the horizontal traces on the buried instrument were over 40 dB quieter than those of the seafloor instrument [Collins *et al.*, 2001; Stephen *et al.*, 2003].

The MOBB package is a permanent ocean observatory composed of a very broadband three-component Guralp CMG-1T broadband seismometer, along with a DPG and two orthogonal seafloor current meters that are aligned with the horizontal seismometer components [Romanowicz *et al.*, 2006, 2009]. The system was emplaced by a remotely operated vehicle and is routinely calibrated with a built-in leveling system. The system is located 40 km offshore Monterey Bay on the western side of the San Gregorio Fault at a water depth of 1036 m and is buried approximately 20 cm beneath the seafloor. We assume that the two horizontal components are closely aligned with N-S and E-W.

In order to explore the relationship between infragravity energy on OBSs and environmental conditions, we inspect weather buoy data. The United States National Oceanographic and Atmospheric Administration (NOAA) maintains buoys throughout the oceans that monitor wind, wave, and other environmental data. We use buoys located in the vicinity of our OBS packages. NOAA buoy 51003 is located 100 km west of OSN1, and NOAA buoy 46042 is 24 km NW of MOBB (see Figures 1 and 2). Here we use NOAA's published mean hourly wind speeds where the wind speed is averaged over an 8 min interval every hour. Previous studies have inferred that high seas and winds lead to higher vertical infragravity power [Dolenc *et al.*, 2005; Wang *et al.*, 2010; Webb *et al.*, 1991]; Ardhuin *et al.* [2014] calculate an empirical parameter relating the height of nearshore infragravity waves with significant wave height and the square of the mean wave period. Little research has been devoted to the correlation between these conditions and horizontal infragravity

deformation. We employ wind, wave, and tide data collected by the NOAA buoys in our investigation. The availability of seafloor current data at MOBB also provides us a unique opportunity to explore the effects of deep-ocean currents on observations of infragravity energy as defined in this paper.

## 4. Data Processing

### 4.1. Coherence and Power Spectra

We use the magnitude-squared coherence between the infragravity pressure signal and horizontal deformation as a measure of horizontal infragravity energy, as it gives a quantitative evaluation of how much of the horizontal acceleration is attributed to infragravity loading. Coherence is given by the equation

$$C_{xy}(f) = \frac{|P_{xy}(f)|^2}{P_{xx}(f)P_{yy}(f)} \quad (6)$$

where  $P_{xx}(f)$  and  $P_{yy}(f)$  are the power spectral densities of the two time series and  $P_{xy}(f)$  is the cross power spectral density between them. To process the data, we cut the time series into 1 h segments and apply a bandpass filter between 1 and 1000 s. Previous studies used data windows ranging from 1024 s to 4096 s or longer [e.g., Crawford *et al.*, 1991; Crawford and Singh, 2008; Crawford, 2004] in order to balance frequency resolution with increased averaging. Dolenc *et al.* [2005] found that 1 day stacks of 1 h pressure displacement transfer functions provide a robust estimate. We adopt this strategy and process 1 h time segments.

Our spectra are computed using the package `psd` [Barbour and Parker, 2014], which is based on the Riedel-Sidorenko minimum bias multiple-taper spectral estimation method [Riedel and Sidorenko, 1995]. Instead of Slepian (also known as discrete prolate spheroidal sequences) tapers, the Riedel-Sidorenko method takes advantage of two families of orthonormal tapers: minimum bias tapers and sinusoidal tapers. The program uses these families to produce power spectral density estimates through an iterative refinement of the optimal number of tapers at each frequency. The number of tapers used varies according to spectral shape: where the spectrum is flat, more tapers are taken and thus higher accuracy is attained at the expense of lower frequency resolution. The reverse is applied in frequency ranges where the spectrum is relatively rough. The program applies smoothing that varies with frequency to minimize the sum of variance and bias at each point. This results in variable resolution and error as a function of frequency but produces robust and stable spectral estimations.

We ensure that the signal is uncorrupted by other sources, including energy from passing teleseisms or instrument spikes. Before analysis, we inspect the U.S. Geological Survey National Earthquake Information Center earthquake catalog and exclude time segments associated with global events with magnitudes  $M_w \geq 6$ . In addition, we exclude time segments for events at regional and local distances (epicentral distance  $< 400$  km) and magnitudes  $M_w \geq 4$ . These segments may have high coherence between the vertical seismometer component and pressure, but the associated signal obeys a different dispersion relation than the IG waves and would therefore contaminate our compliance estimates.

### 4.2. Signal Optimization by Horizontal Component Rotation

An important step in the analysis of horizontal OBS components is to point one of the components toward the direction from which the waves approach. For the sake of simplicity, we assume for now that the horizontal components are aligned with the geographic coordinate system, i.e., one component points N-S (BHN) and the other E-W (BHE). This is essentially the case for MOBB, but not for OSN1B, as we discuss in a later section. To optimize the coherence between horizontal deformation and pressure exerted by IG waves, we rotate the horizontal components until a maximum is found on one component, BS1, and a minimum on the other, BS2. Given the original seismometer components BHN (or BH1 for OSN1B) and BHE (or BH2 for OSN1B), we rotate each component clockwise by an angle  $\alpha$  using the equation

$$\begin{bmatrix} S1 \\ S2 \end{bmatrix} = \begin{bmatrix} \cos \alpha & \sin \alpha \\ -\sin \alpha & \cos \alpha \end{bmatrix} \begin{bmatrix} NS \\ EW \end{bmatrix} \quad (7)$$

For each 1 h data segment we independently find the angle that achieves the highest average coherence in the infragravity band ( $5 \text{ mHz} \leq f \leq 30 \text{ mHz}$ ). We only rotate by angles between 0 and  $180^\circ$ , since a rotation by any angle  $\alpha$  provides the same coherence maximum as a rotation by  $\alpha + 180^\circ$ . We then proceed by

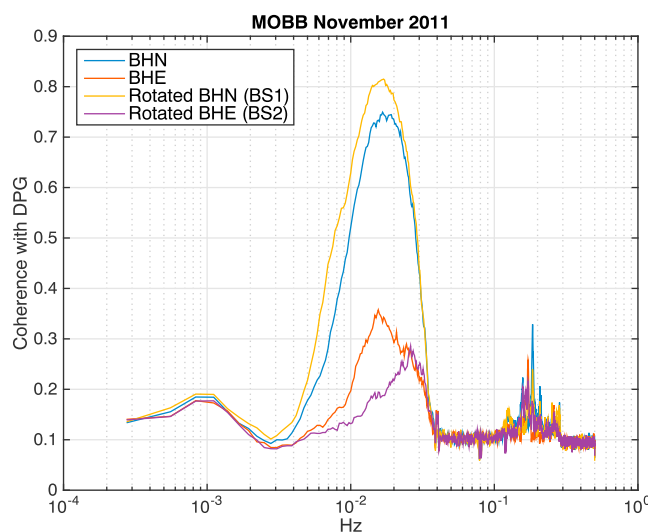


**Figure 4.** Mean coherence of unrotated BHN and BHE traces and rotated BHN (BS1) and rotated BHE (BS2) traces. Mean coherence was determined by processing 1 h time segments and subsequent averaging for the month of November 2011.

analyzing the relationship between various environmental factors and the average horizontal infragravity coherence, which we define as the average coherence value between the DPG and BS1 component in the infragravity band.

Figure 4 illustrates how important this step is. Before rotation, we note that the coherence is much higher for the BHN component than for the BHE component. This indicates that the infragravity waves approach from a northerly direction. However, rotation can further increase coherence for the BHN component (BS1), at the expense of decreasing it for the rotated BHE component (BS2). The implications regarding the rotation angles are discussed in a later section.

## 5. Results

### 5.1. Deep-Ocean Conditions and IG Coherence

Although burial minimizes the tilt noise on OBSs, strong seafloor currents can still influence the coherence between the pressure and the resulting deformation signals. For Figure 5, we determine the mean hourly optimized horizontal IG coherence at station MOBB after rotating the horizontal seismometer components as described in the last section. We also determine the average hourly strength of the current along the seafloor from the two orthogonal current meters. Though the relationship between mean hourly IG coherence and current speeds along the ocean floor is rather diffuse, there is a clear overall negative trend in average coherence as current speed increases. This implies that progressively stronger currents deteriorate the relationship between pressure from IG waves and the resulting horizontal seafloor deformation. A high coherence is rarely achieved when the seafloor current is greater than 20 cm/s, even when the seismometer is buried. We calculate the cross correlation between the current and average coherence as a function of lag to address the question of how quickly the seismometer responds to the currents. Similar tests were previously done by Dolenc *et al.* [2005], Webb *et al.* [1991], and others between vertical coherence and sea surface conditions. The maximum correlation occurs at a lag of zero, indicating an instantaneous response of the package to the current. Ocean bottom currents can induce significant shear stress on the seafloor [Grant and Madsen, 1979; Cacchione and Drake, 1982]. We infer that these current-induced horizontal stresses on the sea bed introduce additional horizontal noise and therefore lower the pressure-seafloor deformation coherence. For completeness sake, we repeated the analysis for the vertical component. Figure 5 clearly demonstrates that the vertical deformation caused by IG waves is much less influenced by deep-ocean currents than the horizontal deformation.

### 5.2. Sea Surface Conditions and IG Coherence

We proceed by investigating the relationship between our observed IG coherence and short-period ocean gravity waves (12–18 s). The underlying assumption here is that ocean gravity waves are generated locally,



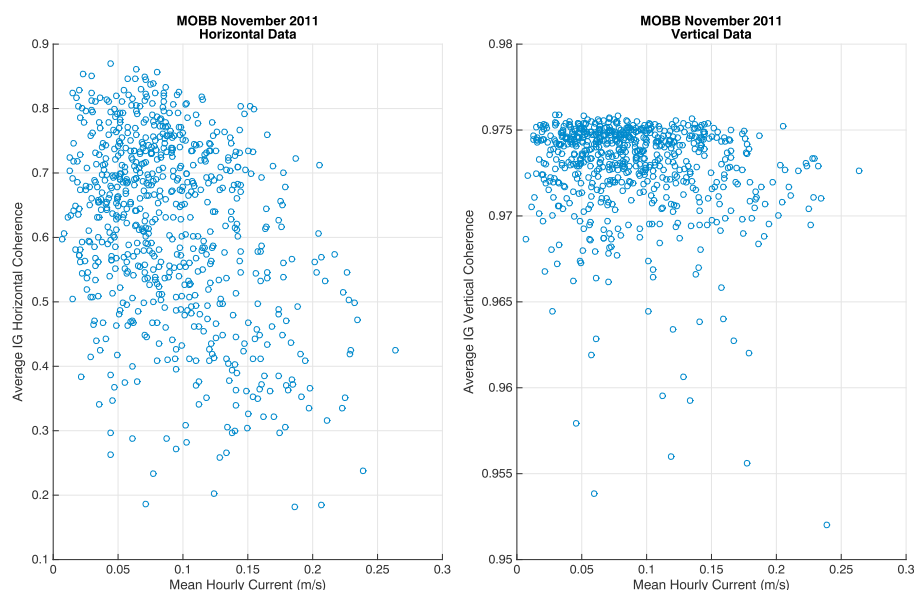


**Figure 5.** Relationship between the strength in deep-ocean currents (expressed as mean hourly current speed) and average IG coherence. (left) For the BS1 component at station MOBB and (right) for the BHZ component at MOBB. Overall, horizontal coherence declines as current speed increases. At the same time, the vertical coherences is less affected. Note that the axis for horizontal coherence is highly compressed.

and wave height correlates with measured wind speeds. We should note that this is a reasonable assumption as ocean swell generated at greater distance typically has a longer period. One of the major outcomes of this analysis is that a strong correlation between horizontal IG coherence and ocean gravity waves suggests that IG waves are generated in coastal environments, in agreement with modern numerical models [Ardhuin *et al.*, 2014]. Using a different approach, previous work on MOBB data found first evidence that this is the case. Dolenc *et al.* [2005] computed power spectral densities (PSD) of the vertical seismometer component for 2003 and 2004. They analyzed infragravity signals during both “quiet” and “stormy” days and investigated the marine conditions that increase the infragravity signal. Their signal was found to correlate positively with significant wave height of short-period ocean gravity waves. Thus, the authors inferred local infragravity

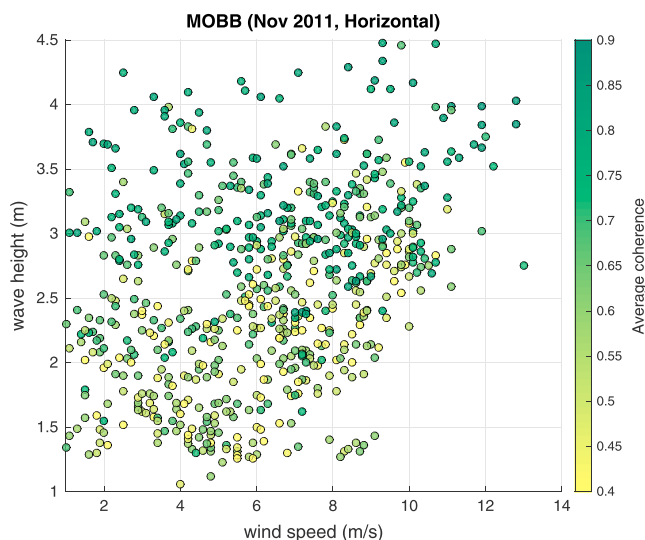


**Figure 6.** Average optimized horizontal IG coherence, as a function of hourly average wind speed and wave height, observed at MOBB and nearby NOAA buoy 46042 during November 2011. The term “optimized” implies that the BS1 component was used.

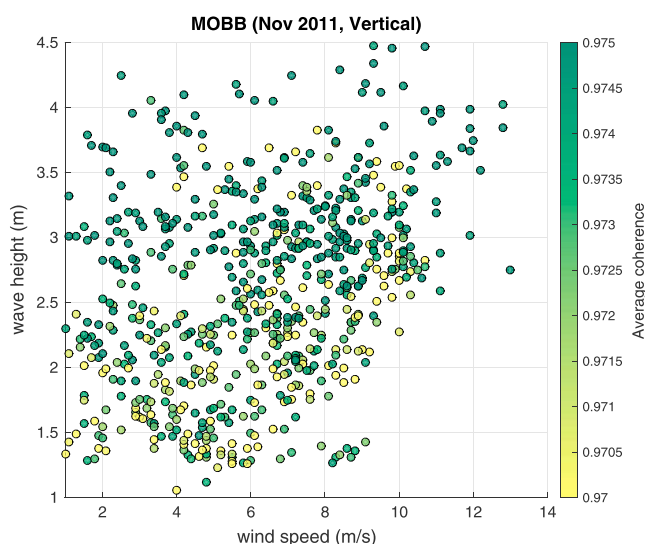


**Figure 7.** Same as Figure 6 but for vertical IG coherence. Note that the color scale in the previous figure is significantly compressed.

wave generation. This supports previous discussions that IG waves have a near-coastal or a shallow-ocean continental shelf origin [e.g., Webb, 1998].

Here we provide an alternative approach through the analysis of horizontal IG coherence. We also provide a wider reference frame by including a test case for the deep ocean, far away from a coast, namely, OSN1B. We examine average infragravity coherence and local sea state for 1 month of OSN1B and MOBB. For the former, we choose April 1998. This choice is controlled by the fact that complete months for OSN1B are available only for March–May 1998. The choice for MOBB, November 2011, is somewhat arbitrary, but this month provides a complete record of sea state data (while April 2012 does not).

We focus on wind data and sea surface gravity waves with periods between 5 and 25 s. Figure 6 displays average optimized horizontal IG coherence, as a function of both mean hourly wave height and hourly average wind speed observed at MOBB during November 2011. We analyze optimized coherence instead of simply spectral power in order to investigate causality and minimize the influence of incoherent noise. The horizontal IG coherence increases as wave height increases. Interestingly, as wind speed increases, wave height also has to increase to produce the same level of coherence though this may be induced intrinsically by the causal effect between local wind speed and wave height. At sustained wind speeds of 10 m/s and above, this linear dependence seems to break down and high horizontal IG coherence is reached for relatively smaller wave heights. A similar trend is observed for vertical IG coherence though much smaller wave heights and wind speeds are required to reach similar levels of coherence (Figure 7).

The situation seems far more complex for deep-ocean station OSN1B (Figures 8 and 9). Note that the IG coherence is significantly lower overall than that at MOBB. No relationship appears to exist between horizontal IG coherence and the local sea state. We currently have no good explanation why coherence is highest for wind speeds of 8 m/s and wave heights of greater than 3 m. The IG coherence is slightly higher for the vertical component overall, but there is no obvious dependence on wind speed and wave height.

We also explore the relationship between horizontal IG coherence and the frequency content in the local sea state, at both OBS locations. Figure 10 confirms the relatively weak relationship at OSN1B between IG coherence and local short-period ocean waves on the one hand, but the strong relationship at MOBB on the other. Maximum coherence is achieved for periods around 15 s, which is actually the dominant period found in swell around MOBB [Dolenc et al., 2005]. The situation at OSN1B is less clear.

Finally, we analyze the relationship between horizontal IG coherence and the total power in the ocean wave spectrum as expressed through the squared spectrum RMS (Figure 11). This figure is complementary to, and essentially confirms findings discussed for Figures 8 and 9. At MOBB, stronger local waves lead to



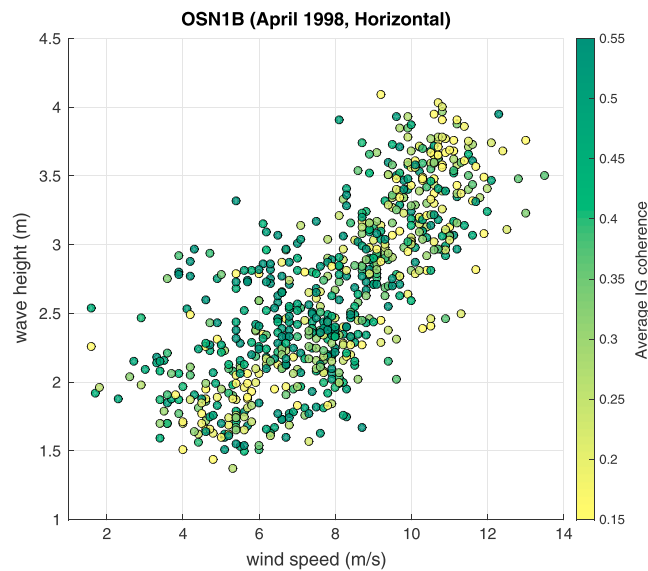


**Figure 8.** Average optimized horizontal IG coherence, as a function of hourly average wind speed and wave height, observed at OSN1B and nearby NOAA buoy 51003 during April 1998. The term “optimized” implies that the BS1 component was used.

higher horizontal IG coherences (though there exists a significant scatter), while at OSN1B no such trend can be found.

To summarize, at MOBB, we find that “stormy” conditions with great wave heights generally lead to higher IG coherence. We take this as an indication that infragravity waves are generated locally, as *Dolenc et al.* [2005, 2007] inferred previously. We find no such strong correlation for OSN1B and infer that the infragravity waves associated with our observations must have been generated elsewhere.

### 5.3. Direction of Approach of IG Waves

In this section, we examine the direction from which IG waves approach at each of the two OBS sites. To do this, we must know the orientation of the horizontal seismometer components. We are fairly confident that the components are roughly aligned with the geographic coordinate system at MOBB, but the orientation at OSN1B is unknown; however, we can determine the orientation during postprocessing of seismic surface waves from distant large earthquakes [e.g., *Laske, 1995; Stachnik et al., 2012*]. Here we determine the alignment of the horizontal components using the Rayleigh wave polarization analysis detailed by

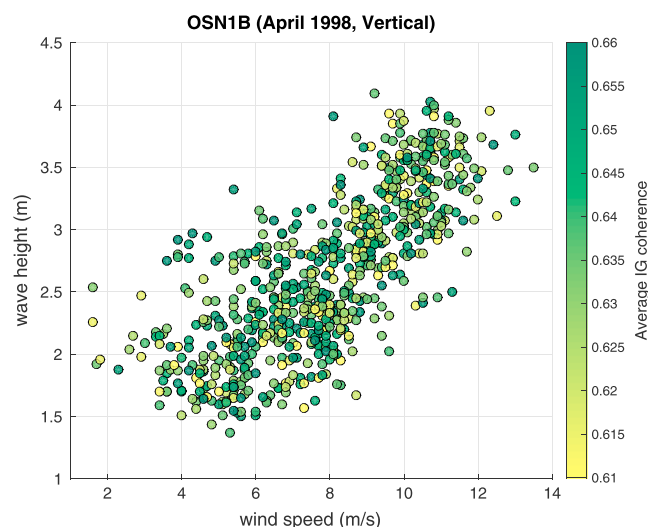


**Figure 9.** Same as Figure 8 but for vertical IG coherence. Note that the color scale in the previous figure is different.

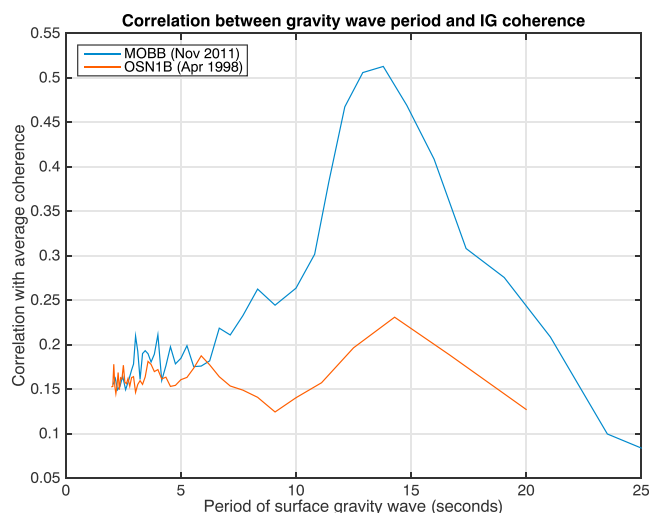


**Figure 10.** Cross correlation between average horizontal IG coherence and period of surface gravity waves, at both OBS stations MOBB and OSN1B, averaged over the respective months noted in previous figures.

Stachnik *et al.* [2012]. Using 32  $M_s \geq 5.5$  global events from the entire 131 days of deployment for OSN1B, we determine the orientation of BH1 to be  $148.1^\circ \pm 1.8^\circ$  clockwise from north. We also check the orientation at MOBB. We use 29  $M_s \geq 5.5$  earthquakes between 1 September 2011 and 2 May 2012. We obtain a slight misalignment with the geographic coordinate system where the orientation of BHN is  $8.1^\circ \pm 3.1^\circ$ . We should mention that we determine the MOBB orientation strictly for the purpose of this study. A more accurate estimate of the alignment at MOBB should include the entire time span over which MOBB has been operational, but we feel that the associated work goes beyond the scope of this paper.

To determine the directionality, we investigate the rotation angles that we obtain when we determined the hourly optimized horizontal IG coherence, now under consideration of the misalignment of the horizontal seismometer components as found in the teleseismic reorientation work (Figure 12). We take these rotation

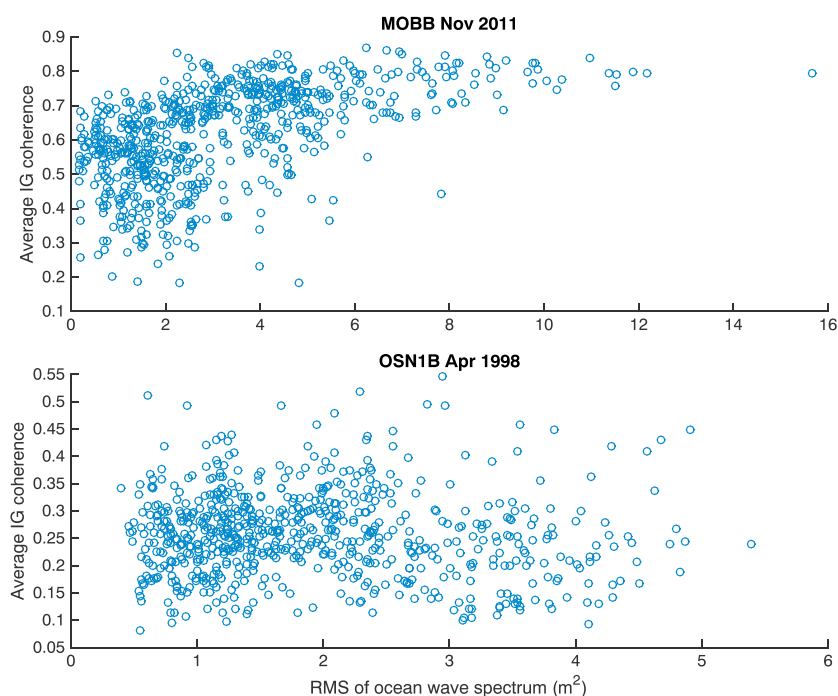


**Figure 11.** Hourly averaged horizontal IG coherence as function of power in the wave spectrum, for the moths noted in previous figures. (top) MOBB; (bottom) at OSN1B.

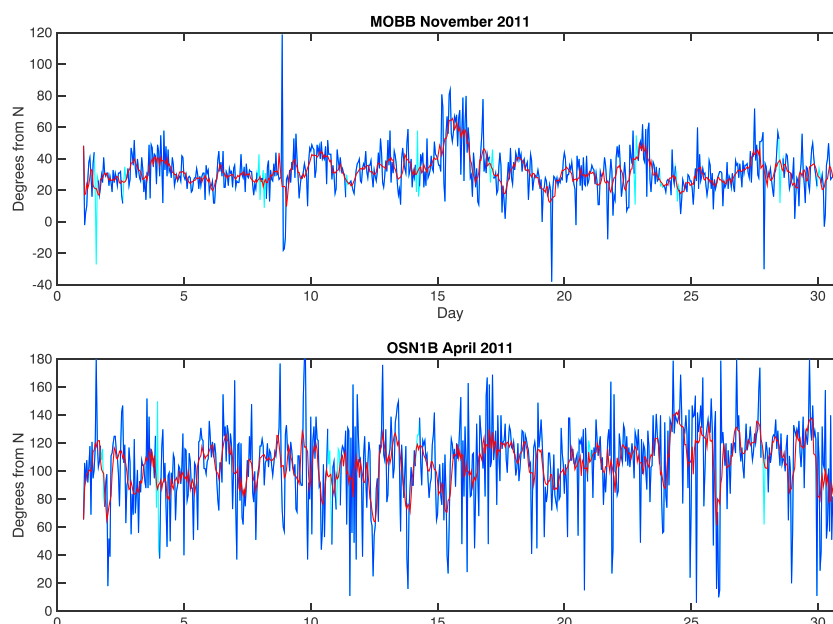


**Figure 12.** Rotation angles obtained during the optimization process for horizontal IG coherence, as a function of time, for both OBS stations used in this study. The rotation angles have not been corrected for instrument orientation. The light blue segments are rotation angles that may have been corrupted by transient seismic energy and are excluded from our analyses. The red line tracks a running mean computed using 6 hour intervals.

angles to be the direction of approach of the IG waves. Analysis of the corresponding horizontal seismic power spectra and particle motion plots confirms this (not shown).

We observe a fairly stable raw infragravity azimuth of  $\approx 30^\circ$  clockwise from north at station MOBB. A correction for instrument misorientation would place the angle of approach at around  $38^\circ$ . Although the rotation analysis inherently includes a  $180^\circ$  ambiguity, we believe this indicates that the majority of infragravity waves are sourced from Monterey Bay and the local continental shelf where short-period surface gravity waves interfere in a nonlinear fashion. The rotation angles for OSN1B exhibit significantly higher variance, but a general azimuth of approximately  $110^\circ$ , corresponding to either  $258^\circ$  or  $78^\circ$  after correcting for instrument orientation (recall that BH1 is oriented  $148.1^\circ$  clockwise from north). Seventy-eight degrees is approximately the azimuth between the OBS and the narrow shelf off the north coast of the island of Hawaii. It is worth noting that there is a 2 km drop in the seafloor across the edge of the shelf. While infragravity energy observed at OSN1B may not be generated locally, it may well be generated on the Hawaiian shelf and propagate to the OBS site. The variance of the angles and the weakness of the coherence suggests that the IG energy is also approaching from many other angles as well. Figures 1 and 2 give a qualitative depiction of the infragravity wave source directions inferred at both sites.

Figure 12 includes a 6 h running mean for each of the angle time series. At MOBB, several periods of sustained deviation from the median rotation angle can be seen, with the strongest occurring on day 15. While we find no relationship between local weather conditions and these arrival angle excursions, the angle deviation from the median exhibits strong negative correlation with the average coherence. We interpret this to indicate that the infragravity wave field during these periods is strongly influenced by IG waves generated in a different source region, likely by a storm elsewhere in the Pacific. The larger scatter in the Figure 12 for OSN1B may be explained by the relatively low local wave power. To investigate this, we plot the rotation angles as function of RMS of the wave spectrum (Figure 13). At OSN1B, rotation angles are widely scattered as a function of RMS, and no significant trends are apparent. On the other hand, at MOBB, we observe that the variance of the rotation angle decreases as the energy in the ocean wave spectrum increases. Note, however, that RMS values at OSN1B never reach those at MOBB.

We have thus far only considered the rotation angle that maximizes the average coherence in the entire infragravity band. We may gain additional insight into the internal variability of IG waves by calculating the optimal rotation angle for each frequency individually. Figure 14 displays a polar histogram detailing the directional

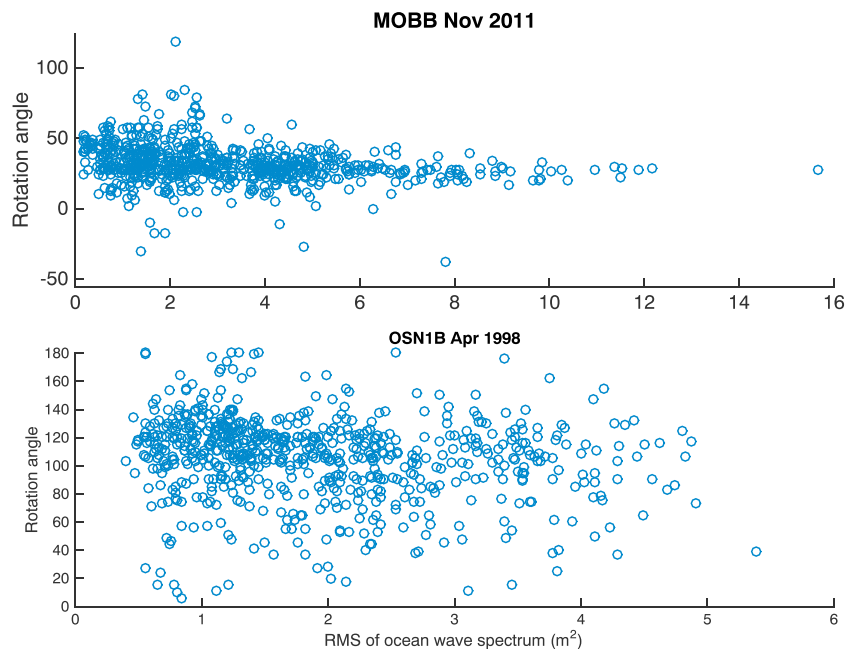


**Figure 13.** The same rotation angles in Figure 12 but now as a function of RMS in the local wave spectrum. Note the different scales in the x axes.

distribution for two different hours at MOBB on 1 November 2011. Note that this day is within a time span that provided fairly stable rotation angles in Figure 12. As is evident from both panels, the internal consistency of direction of approach can vary greatly. During hour 10, most sampled frequencies share similar angles implying that IG waves consistently came from the same direction (roughly  $40^\circ$ ). During hour 3, angles are much more distributed, which may indicate that waves of different periods came from different directions or that IG wave activity was generally lower, leading to less coherent wave packets. Hour 10 also coincides with a higher mean wave height (3.6 m versus 2.7 m) and higher average coherence (0.71 versus 0.49), suggesting that coherence is optimized during periods of consistent and unidirectional infragravity wave propagation. In general, hours with higher variance in the calculated angles exhibit lower average infragravity coherence.

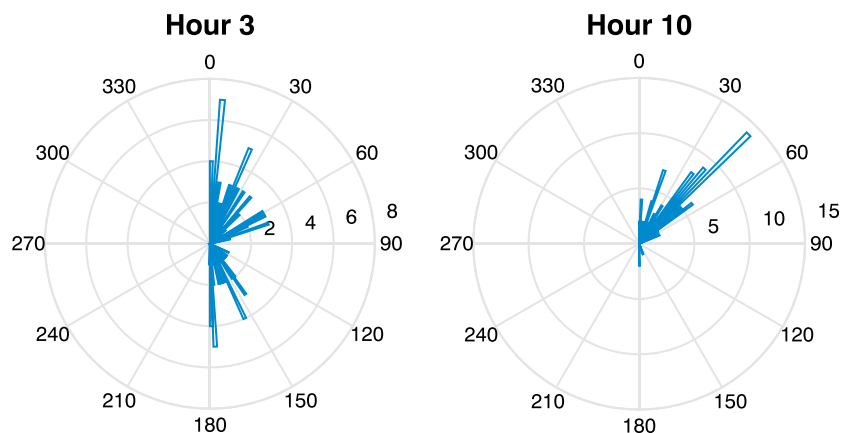


**Figure 14.** Polar representation of histograms of rotation angles (implied direction of IG wave approach) at MOBB, as a function of individual frequency, sampled at 100 frequencies between 1 and 30 mHz. The two panels show histograms for hours 3 and 10 on 1 November 2011 (corresponding to 8 P.M. and 3 A.M. local time). Note the different radial scales in both panels.

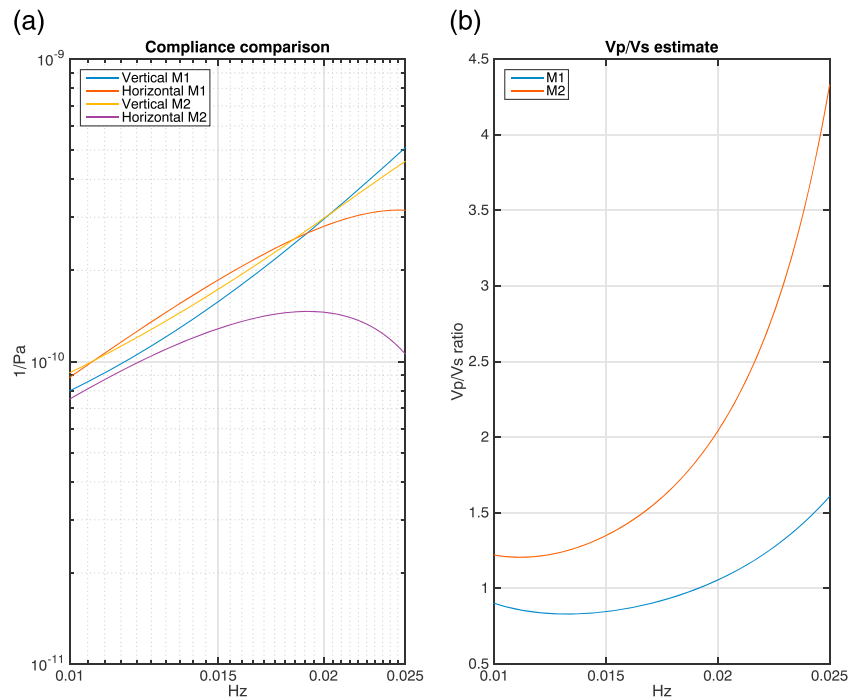


**Figure 15.** Compliance forward modeling of two structures with similar vertical compliance values but differing horizontal values. (a) Comparison of the different compliance values obtained. (b) The ratio of vertical to horizontal compliance, which may give an estimate of the  $V_p/V_s$  ratio.

## 6. Discussion

### 6.1. Horizontal Seafloor Compliance

Although a full analysis is beyond the scope of this paper, our ultimate goal is the use of horizontal infragravity energy in a seafloor compliance inversion. Seafloor compliance is defined as the transfer function between displacement and pressure and was first developed as a tool to study shallow shear structure (<10 km) in the deep oceans by Crawford *et al.* [1991]. Recent advances have improved compliance capabilities with regards to both modeling [e.g., Iassonov and Crawford, 2008; Zha *et al.*, 2014] and imaging [e.g., Willoughby *et al.*, 2008; Crawford and Singh, 2008]. High-quality coherent pressure and horizontal displacement data would allow us to perform a horizontal compliance inversion for subsurface structure.

Significant developments are necessary in horizontal compliance theory before a meaningful inversion can be done. While vertical acceleration due to infragravity waves is always  $180^\circ$  out of phase with the pressure signal, the phase of the horizontal acceleration is dependent on frequency and Earth model [Webb, 1998]; however, horizontal compliance measurements would provide significant additional constraints on local subsurface structure. A joint inversion of horizontal and vertical compliance data would provide tighter bounds on a final model and remove some of the inherent ambiguity of vertical compliance modeling. Figure 15a shows the results for forward modeling for two simple crustal structures with very similar vertical compliance values but horizontal compliance values that differ by a factor of three at higher frequencies. The two models represent typical oceanic crustal structure overlain by 1 km of sediment, and only the upper 500 m differ in elastic parameters. Including horizontal compliance can increase the resolving power of an inversion. Additionally, as described by Crawford [2004], the ratio of vertical to horizontal compliance provides an estimate of the  $V_p/V_s$  ratio. The quasi-static 1-D solution for an elastic half-space (from equation (3)) states

$$\frac{\eta_z}{\eta_H} = \frac{(\lambda + 2\mu)/(2\mu(\lambda + \mu))}{1/2(\lambda + \mu)} = \frac{\lambda + 2\mu}{\mu} = \frac{\alpha^2}{\beta^2} \quad (8)$$

From this result we expect vertical compliance to always exceed horizontal compliance, but in some realistic Earth structures this relationship may be voided. As seen in Figure 15b, one of the models produces expected compliance values that broadly agrees with the  $V_p/V_s$  ratios present in the starting model, while the relationship only holds at high frequencies for the other model.

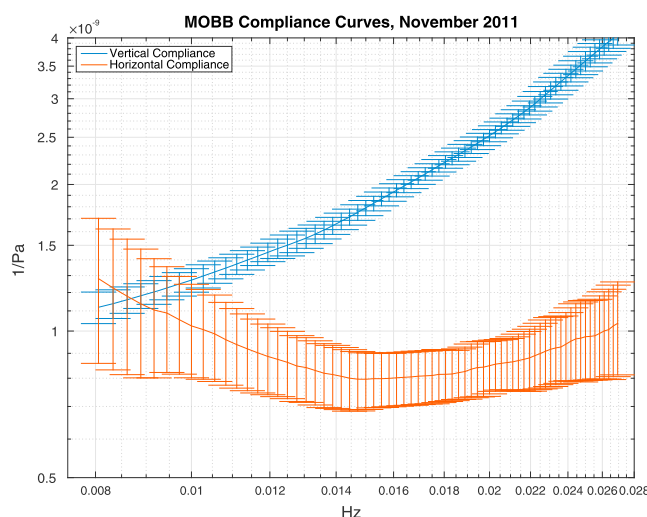


**Figure 16.** Calculated MOBB compliance curves for November 2011.

The directionality measurements also suggest the possibility of detecting anisotropy from horizontal compliance measurements. Periods of sustained infragravity energy arrival angle deviation may yield different compliance curves, which could be inverted for directionally dependent velocities. We examined several extended periods with significantly different dominant infragravity directions at both MOBB and OSN1B but were unable to identify a statistically significant azimuthal dependence for the horizontal compliance values, indicating that local anisotropy is either negligible or beneath our limits of detection; however, this does not preclude the possibility at other locations with stronger anisotropy or more precise measurements.

Figures 16 and 17 display the horizontal and vertical compliance curves calculated at MOBB and OSN1B, respectively. The functions diverge due to distinct sensitivities to the underlying structure. While the MOBB compliance data are consistent with our expectations, the values at OSN1B appear inverted, as the horizontal signal is greater than the vertical. *Araki et al.* [2004] observe this phenomenon at sealed borehole seismometers offshore Japan. The authors do not report the coherence between pressure and deformation (owing to the absence of a collocated pressure gauge at the sites) but conclude that the signal is caused by compliance-induced tilting. In that location, the local geology was inferred from borehole logging, and a higher vertical compliance was expected from the starting model; this may not be the case at OSN1B. The borehole logs obtained at site OSN1 (approximately 300 m from OSN1B) indicate 242 m of soft sediment overlying crystalline basement [Dziewonski *et al.*, 1992b]. We can model an inverted signal similar to the

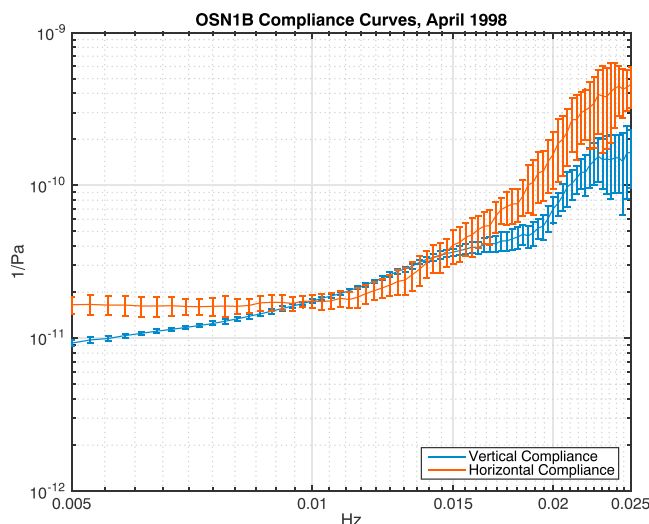


**Figure 17.** Calculated OSN1B compliance curves for April 1998.



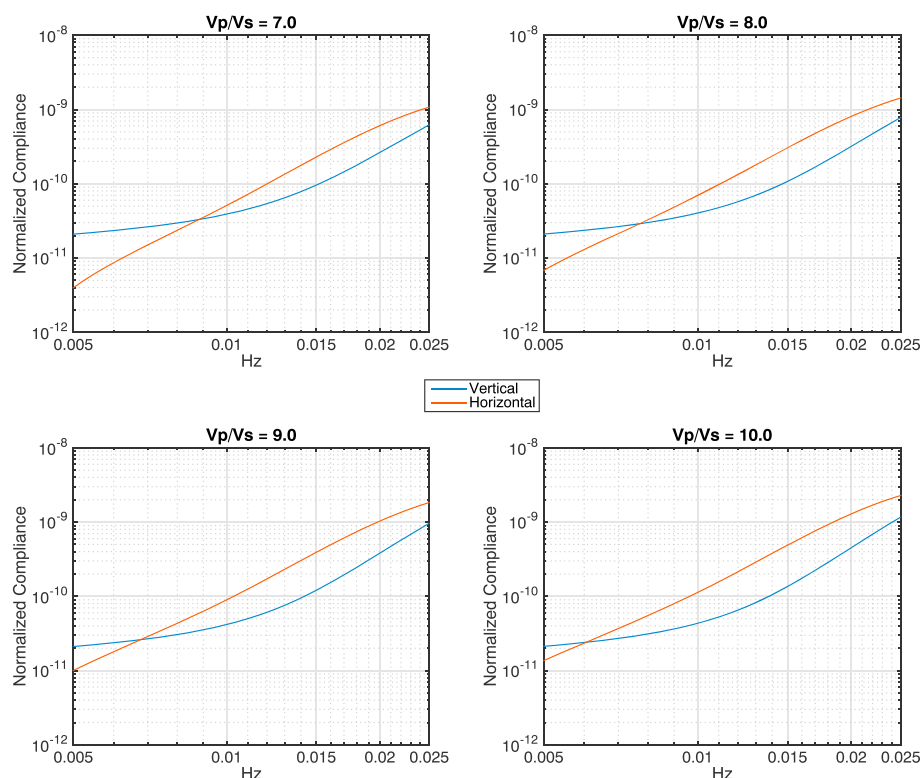


**Figure 18.** Forward modeling of OSN1B compliance. All models have fixed structure typical of oceanic crust and are overlain by 250 m of sediment. Only the sedimentary shear velocity varies. A sharp contrast between sediment and bedrock  $V_p/V_s$  ratios can produce a higher expected horizontal compliance signal than vertical.

one calculated at OSN1B using a sharp shear velocity interface between the thin sediments and the basalt. Figure 18 plots four possible structures, each with standard oceanic crust overlain by 250 m of sediment. The density and compressional speed of the sediments are fixed (at 1.6 g/cc and 1.7 km/s, respectively, in agreement with the ODP borehole logs), while the  $V_p/V_s$  ratio varies between 7.0 and 10.0. Sediments with velocity ratios of this magnitude are not uncommon in marine environments: *Hamilton* [1979] reports a 1000 m sedimentary package with  $V_p/V_s$  ratios ranging from 2.6 at the base to 13 and greater at the seafloor. In the OSN1B environment, a higher horizontal compliance is possible. The lower relative BH1-DPG coherence at OSN1B may bias the results as well, but we believe this to be unlikely. We calculate compliance using data from all 131 days of the deployment and obtain nearly identical results as the ones presented here. The low coherence is likely due to the higher instrument response roll-off at OSN1B and to infragravity waves from different source azimuths destructively interfering. All of this leads us to have confidence that we are indeed observing horizontal compliance at both MOBB and OSN1B.

## 6.2. Removing Long-Period Noise to Lower Earthquake Detection Thresholds

The primary use of OBS recordings is earthquake detection and waveform analysis. The detection threshold of teleseismic events has been reported as consistently higher on OBSs than on land instruments [e.g., *Webb*, 1998], especially when analyses rely on the horizontal seismometer components. The problem is particularly acute in the infragravity band, where noise sources are entirely absent on most land stations (though clearly visible on some island stations [*Rhie et al.*, 2008]). A reduction of the long-period infragravity signal on vertical OBS components has been done successfully through deconvolution of the pressure signal from the ground acceleration [*Crawford and Webb*, 2000; *Crawford et al.*, 2006; *Taira et al.*, 2014]. This process has started to become a routine part of preprocessing OBS vertical components [*Dolenc et al.*, 2007; *Taira et al.*, 2014], particularly for the waveforms gathered for the recent community OBS deployment in Cascadia. With a coherent horizontal signal, we hope to eventually apply similar procedures to horizontal components, at least on buried OBSs.

### 6.3. Other Buried OBS Sites

While the two OBS deployments discussed in this paper are the only ones that we analyzed, they are not the only ones with buried seismometers. The French borehole experiment OFM (Observatoire Fond de Mer) conducted in 1992 provides promising seismic data but lacked a DPG [Montagner *et al.*, 1994; Beauduin and Montagner, 1998]. We therefore cannot conduct a corresponding study for that deployment. We note that although some vertical infragravity energy is visible on their published spectra, the horizontal components appear to be too noisy for our purposes. A “corehole” seismic experiment run in 1996 and 1997 in Monterey Bay produced very low-noise records [Stakes *et al.*, 1998], but the limited bandwidth of the deployed sensors does not seem to allow a study as ours since the instrument response of that seismometer seems to imply high-quality data only at frequencies above 0.1 Hz. The H<sub>2</sub>O experiment halfway between Hawaii and the U.S. West Coast between 1999 and 2003 was composed of a three-component seismometer and a pressure-sensing hydrophone buried in 0.4 m of seafloor, but high long-period noise rendered infragravity energy, both vertical and horizontal, difficult or impossible to measure [Duennebie *et al.*, 2002].

The NEREID deployment mentioned previously [Araki *et al.*, 2004] consisted of four borehole observatories installed offshore Japan. The three-component seismometers were cemented in the borehole to maximize coupling and to avoid flow effects that influenced long-period data of previous borehole deployments [Collins *et al.*, 2001]. The authors report clear infragravity wave energy on both the horizontal and vertical components, but lack a collocated differential pressure gauge. The goal of the study was to minimize infragravity noise in order to maximize the effectiveness of event analysis, and the authors find that the strongest infragravity signal is found on instruments in the sediment.

## 7. Summary

We observe consistent infragravity energy on the horizontal components of two buried OBS stations: MOBB and OSN1B. These two sites are in vastly different ocean settings: MOBB is located in a nearshore environment at 1000 m depth, while OSN1B was deployed in the deep open ocean far away from any continental coast. Infragravity waves are not routinely observed on the horizontal components of traditional seafloor OBSs because current-related tilt noise overpowers the signal; sensor burial is necessary for our observations. We choose to measure infragravity energy using the coherence between the pressure signal exerted by infragravity waves on the seafloor (as measured by a broadband pressure sensor) and horizontal seafloor deformation (as measured by a broadband seismometer). Collocating both types of sensors ensures that the horizontal deformations we observe can be attributed to passing infragravity waves. The coherence between the signals also gives us a reliable quantitative measurement of the signal-to-noise ratio of our observations.

The positive correlation between horizontal infragravity wave measurements and short-period ocean gravity waves can provide evidence for a nearshore origin where nonlinear constructive interference of the local swell leads to the generation of long-period infragravity waves. The strong correlation between infragravity energy observed at MOBB, as opposed to the weak correlation seen at OSN1B, argues for such a generating mechanism. Our analysis of rotation angles obtained through the optimization process for horizontal IG energy also provides strong evidence that infragravity waves can be generated by near-coastal swell.

We plan to use the observations discussed in this paper in a forthcoming inversion of vertical and horizontal compliance. The horizontal compliance method is not identical to vertical compliance and additional theoretical development is necessary, but the combined results should provide more robust constraints on sedimentary and crustal structure. In case of disagreement, we hope to investigate near-surface anisotropy (transverse isotropy). The results of our IG source directionality analysis imply that horizontal compliance may be best characterized in regions of unidirectional IG propagation where destructive interference is avoided and high DPG-BH1 coherence can be achieved.

Another promising avenue for horizontal compliance studies are long-term traditional OBS deployments. The PLUME experiment [Laske *et al.*, 2009; Wolfe *et al.*, 2009] consisted of 74 marine instruments, each deployed for approximately 12 months between 2005 and 2007. These are seafloor instruments that suffer from the high tilt-induced long-period horizontal noise that buried instruments lack, but the long duration of the deployments allows us to stack thousands of transfer functions, thus possibly revealing a coherent horizontal compliance signal. Initial results show that with 12 months of continuous data, enough transfer functions can be obtained to give an estimate of horizontal compliance with reasonable uncertainties.

Ruan *et al.* [2014] recently introduced a method of crustal imaging using the vertical displacement-pressure transfer function in the microseism frequency range (0.1–0.2 Hz). While using similar techniques as seafloor compliance, the displacement is caused by microseism-generated Rayleigh waves rather than water wave forcing. The microseism spectrum at any location depends on local and distant ocean wave spectra, as well as the directional spectrum of the ocean waves [Webb, 1992]. Like infragravity compliance, the method depends on high coherence between the displacement and pressure spectra. While common using vertical traces, high coherence is rarely attained from horizontal recordings. We attempt to improve coherence between the pressure and the horizontal spectra using similar weather conditions and a rotation analysis as previously described but are unable to achieve significant signal coherence. This may have implications for microseism propagation and generation, as well as intermediate-period horizontal noise.

## Appendix A: OSN1B Instrument Responses

Instrument responses for modern seismic instrumentation are traditionally presented in a poles and zeros format, satisfying the following transfer function in the frequency domain:

$$T(\omega) = k \frac{(i\omega - z_1)(i\omega - z_2)(i\omega - z_3)\dots}{(i\omega - p_1)(i\omega - p_2)(i\omega - p_3)\dots} \quad (\text{A1})$$

where  $z_n$  are the zeros,  $p_n$  are the poles, and  $k$  is a combined normalization factor that includes the polynomials for the numerator and denominator as well as the data logger response. The parameter values are listed in Tables A1 through A4.

**Table A1.** Response Parameters Used for OSN1B DPG

Zeros	Poles	Sensitivity
0.00 + 0.00i	−3.00e − 02 + 0.00i	−1.02e + 06
0.00 + 0.0i	−5.75e01 + 0.0i	
−1.03e04 + 0.0i	−1.0e02 + 0.0i	
	−2.0e − 01 + 0.0i	
	−2.87e02 + 0.0i	

**Table A2.** Response Parameters Used for OSN1B BHZ

Zeros	Poles	Sensitivity
0.00 + 0.00i	−5.90e − 03 − 5.90e − 03i	−3.65e + 10
0.00 + 0.0i	−5.90e − 03 + 5.90e − 03i	
1.47e02 + 0.0i	−7.32e01 + 3.76e01i	
0.00 + 0.00i	−7.32e01 − 3.76e01i	

**Table A3.** Response Parameters Used for OSN1B BH1

Zeros	Poles	Sensitivity
0.00 + 0.00i	−5.90e − 03 − 5.90e − 03i	−3.67e + 10
0.00 + 0.0i	−5.90e − 03 + 5.90e − 03i	
1.47e02 + 0.0i	−7.32e01 + 3.76e01i	
0.00 + 0.00i	−7.32e01 − 3.76e01i	

**Table A4.** Response Parameters Used for OSN1B BH2

Zeros	Poles	Sensitivity
0.00 + 0.00i	−5.90e − 03 − 5.90e − 03i	−3.66e + 10
0.00 + 0.0i	−5.90e − 03 + 5.90e − 03i	
1.47e02 + 0.0i	−7.32e01 + 3.76e01i	
0.00 + 0.00i	−7.32e01 − 3.76e01i	

## Acknowledgments

This research was supported by NSF grants EAR-11-13075 and EAR-14-15763. We wish to thank the operators of the Monterey Ocean Bottom Broadband Seismometer (MOBB), whose waveform data and metadata are accessible through the Northern California Earthquake Data Center (NCEDC). The facilities of IRIS Data Services, and specifically the IRIS Data Management Center, were used for access to Ocean Seismic Network (OSN) waveforms and related metadata used in this study. We thank John Collins for providing instrument responses and related codes. Figures 1 and 2 were generated using Generic Mapping Tools 4.5 [Wessel and Smith, 1991; Wessel et al., 2013]. We thank Wayne Crawford for compliance forward modeling codes. We also thank Crawford, Michael Walter and an anonymous reviewer for constructive comments that led to significant manuscript improvement.

## References

- Abel, J. (1987), *Principles of Ocean Physics*, Academic Press, San Diego, Calif.
- Araki, E., M. Shinohara, S. Sacks, A. Linde, T. Kanazawa, H. Shiobara, H. Mikada, and K. Suyehiro (2004), Improvement of seismic observation in the ocean by use of seafloor boreholes, *Bull. Seismol. Soc. Am.*, *94*(2), 678–690.
- Ardhuin, F., A. Rawat, and J. Aucan (2014), A numerical model for free infragravity waves: Definition and validation at regional and global scales, *Ocean Model.*, *77*, 20–32.
- Aucan, J., and F. Ardhuin (2013), Infragravity waves in the deep ocean: An upward revision, *Geophys. Res. Lett.*, *40*, 3435–3439, doi:10.1002/grl.50321.
- Barbour, A., and R. Parker (2014), PSD: Adaptive, sine multitaper power spectral density estimation for R, *Comput. Geosci.*, *63*, 1–8.
- Beauduin, R., and J. P. Montagner (1998), Time evolution of broadband seismic noise during the french pilot experiment OFM/SISMOBS, *Geophys. Res. Lett.*, *23*(21), 2995–2998.
- Bromirski, P. D., O. V. Sergienko, and D. R. MacAyeal (2010), Transoceanic infragravity waves impacting antarctic ice shelves, *Geophys. Res. Lett.*, *37*, L02502, doi:10.1029/2009GL041488.
- Cacchione, D., and D. Drake (1982), Measurements of storm-generated bottom stresses on the continental shelf, *J. Geophys. Res.*, *87*(C3), 1952–1960.
- Collins, J., F. Vernon, J. Orcutt, R. Stephen, K. Peal, F. Wooding, F. Spiess, and J. Hildebrand (2001), Broadband seismology in the oceans: Lessons from the oceans seismic network pilot experiment, *Geophys. Res. Lett.*, *28*(1), 49–52.
- Cox, C., T. Deaton, and S. Webb (1984), A deep-sea differential pressure gauge, *J. Atmos. Oceanic Technol.*, *1*, 237–246.
- Crawford, W., and S. Singh (2008), Sediment shear properties from seafloor compliance measurements: Faroes-shetland basin case study, *Geophys. Prospect.*, *56*, 313–325.
- Crawford, W., S. Webb, and J. Hildebrand (1991), Seafloor compliance observed by long-period pressure and displacement measurements, *J. Geophys. Res.*, *96*(B10), 151–160.
- Crawford, W., S. Webb, and J. Hildebrand (1998), Estimating shear velocities in the oceanic crust from compliance measurements by 2-D finite difference modeling, *J. Geophys. Res.*, *103*(B5), 9895–9916.
- Crawford, W., S. Webb, and J. Hildebrand (1999), Constraints on melt in the lower crust and Moho at the East Pacific rise using seafloor compliance measurements, *J. Geophys. Res.*, *104*(B2), 2923–2939.
- Crawford, W., V. Ballu, X. Bertin, and M. Karpytchev (2015), The sources of deep ocean infragravity waves observed in the North Atlantic Ocean, *J. Geophys. Res. Oceans*, *120*, 5120–5133, doi:10.1002/2014JC010657.
- Crawford, W. C. (2004), The sensitivity of seafloor compliance measurements to sub-basalt sediments, *Geophys. J. Int.*, *157*, 1130–1145.
- Crawford, W. C., and S. Webb (2000), Identifying and removing tilt noise from low-frequency (less than 0.1 Hz) seafloor vertical seismic data, *Bull. Seismol. Soc. Am.*, *90*(4), 952–963.
- Crawford, W. C., R. A. Stephen, and S. T. Bolmer (2006), A second look at low-frequency marine vertical seismometer data quality at the OSN-1 site off Hawaii for seafloor, buried, and borehole emplacements, *Bull. Seismol. Soc. Am.*, *96*(5), 1952–1960.
- Dolenc, D., B. Romanowicz, D. Stakes, and P. McGill (2005), Observations of infragravity waves at the Monterey Ocean Bottom Broadband station (MOBB), *Geochem. Geophys. Geosyst.*, *6*, Q09002, doi:10.1029/2005GC000988.
- Dolenc, D., B. Romanowicz, R. Uhrhammer, P. McGill, D. Neuhauser, and D. Stakes (2007), Identifying and removing noise from the Monterey Ocean Bottom Broadband seismic station (MOBB) data, *Geochem. Geophys. Geosyst.*, *8*, Q02005, doi:10.1029/2006GC001403.
- Duennebie, F., and G. Sutton (1995), Fidelity of ocean bottom seismic observations, *Mar. Geophys. Res.*, *17*, 535–555.
- Duennebie, F., and G. Sutton (2007), Why bury ocean bottom seismometers?, *Geochem. Geophys. Geosyst.*, *8*, Q02010, doi:10.1029/2006GC001428.
- Duennebie, F., D. Harris, J. Jolly, J. Babinec, D. Copson, and K. Stiffel (2002), The Hawaii-2 observatory seismic system, *IEEE J. Oceanic Eng.*, *47*(2), 212–217.
- Dziwonski, A., R. Wilkens, J. Firth, and S. S. Party (1992a), Background and objectives of the ocean seismographic network and leg 136 drilling results, in *Proceedings of the Ocean Drilling Program Initial Report*, vol. 136, pp. 2–8, Ocean Drilling Program, College Station, Tex.
- Dziwonski, A., R. Wilkens, and J. Firth (1992b), Site 843, in *Proceedings of the Ocean Drilling Program Initial Reports*, vol. 136, pp. 65–99, Ocean Drilling Program, College Station, Tex.
- Godin, O., N. Zabolin, A. Sheehan, Z. Yang, and J. Collins (2013), Power spectra of infragravity waves in the deep ocean, *Geophys. Res. Lett.*, *40*, 2159–2165, doi:10.1002/grl.50418.
- Godin, O., N. Zabolin, A. Sheehan, and J. Collins (2014), Interferometry of infragravity waves off New Zealand, *J. Geophys. Res. Oceans*, *119*, 1103–1122, doi:10.1002/2013JC009395.
- Godin, O. A., and I. M. Fuks (2012), Transmission of acoustic-gravity waves through gas-liquid interfaces, *J. Fluid Mech.*, *709*, 313–340.
- Grant, W., and O. Madsen (1979), Combined wave and current interaction with a rough bottom, *J. Geophys. Res.*, *84*(C4), 1797–1808.
- Hamilton, E. (1979),  $V_p/V_s$  and Poisson's ratios in marine sediments and rocks, *J. Acoust. Soc. Am.*, *66*(4), 1093–1101.
- Herbers, T., S. Elgar, and R. Guza (1995a), Generation and propagation of infragravity waves, *J. Geophys. Res.*, *100*(C12), 24,863–24,872.
- Herbers, T., S. Elgar, R. Guza, and E. Thornton (1995b), Infragravity-frequency (0.005–0.05 Hz) motions on the shelf. Part II: Free waves, *J. Phys. Oceanogr.*, *25*, 1063–1079.
- Iassonov, P., and W. Crawford (2008), Two-dimensional finite-difference model of seafloor compliance, *Geophys. J. Int.*, *174*, 525–541.
- Laske, G. (1995), Global observation of off-great-circle propagation of long-period surface waves, *Geophys. J. Int.*, *123*, 245–259.
- Laske, G., J. Collins, C. Wolfe, S. Solomon, R. Detrick, J. Orcutt, D. Berovici, and E. Hauri (2009), Probing the Hawaiian hot spot with new ocean bottom instruments, *EOS Trans. AGU*, *90*(41), 362–363.
- Montagner, J.-P., et al. (1994), The french pilot experiment OFM-SISMOBS: First scientific results on noise level and event detection, *Phys. Earth Planet. Int.*, *84*, 321–336.
- Munk, W. H. (1949), Surf beats, *30*, 849–854.
- Rhie, J., and B. Romanowicz (2006), A study of the relation between ocean storms and the Earth's hum, *Geochem. Geophys. Geosyst.*, *7*, Q10004, doi:10.1029/2006GC001274.
- Rhie, J., D. Dolenc, and B. Romanowicz (2008), Long-period seismic noise at the Farallon Islands: Island's tilting due to infragravity waves as a possible source of Earth's horizontal hum, Abstract S34A-05 presented at 2008 Fall Meeting, AGU, San Francisco, Calif., Dec.
- Riedel, K., and A. Sidorenko (1995), Minimum bias multiple taper spectral estimation, *IEEE Trans. Signal Process.*, *43*, 188–195.
- Romanowicz, B., D. Stakes, D. Dolenc, D. Neuhauser, P. McGill, R. Uhrhammer, and T. Ramirez (2006), The Monterey Bay broadband ocean bottom seismic observatory, *Ann. Geophys.*, *49*, 607–623.
- Romanowicz, B., P. McGill, D. Neuhauser, and D. Dolenc (2009), Acquiring real time data from the Broadband Ocean Bottom Seismic Observatory at Monterey Bay (MOBB), *Seismol. Res. Lett.*, *80*(2), 197–202.

- Ruan, Y., D. Forsyth, and S. Bell (2014), Marine sediment shear velocity structure from the ratio of displacement to pressure of Rayleigh waves at seafloor, *J. Geophys. Res. Solid Earth*, 119, 6357–6371, doi:10.1002/2014JB011162.
- Stachnik, J., A. Sheehan, D. Zietlow, Z. Yang, J. Collins, and A. Ferris (2012), Determination of New Zealand ocean bottom seismometer orientation via Rayleigh-wave polarization, *Seismol. Res. Lett.*, 83, 704–712.
- Stakes, D., J. McClain, T. VanZandt, P. McGill, and M. Begnaud (1998), Corehole seismometer development for low-noise seismic data in a long-term seafloor observatory, *Geophys. Res. Lett.*, 25(14), 2745–2748.
- Stephen, R., F. Spiess, J. Collins, J. Hildebrand, J. Orcutt, K. Peal, F. Vernon, and F. Wooding (2003), Ocean seismic network pilot experiment, *Geophys. Res. Lett.*, 4(10), 1092, doi:10.1029/2002GC000485.
- Taira, T., Z. Zheng, and B. Romanowicz (2014), On the systematic long-period noise reduction on ocean floor broadband seismic sensors collocated with differential pressure gauges, *Bull. Seismol. Soc. Am.*, 104(1), 247–259.
- Tucker, M. (1950), Surf beats: Sea waves of 1 to 5 min. period, *Proc. R. Soc. London, A*(202), 565–573.
- Wang, J.-H., W.-C. Chi, R. N. Edwards, and E. Willoughby (2010), Effects of sea states on seafloor compliance studies, *Mar. Geophys. Res.*, 31, 99–107.
- Webb, S. (1992), The equilibrium oceanic microseism spectrum, *J. Acoust. Soc. Am.*, 92(4), 2141–2158.
- Webb, S., X. Zhang, and W. Crawford (1991), Infragravity waves in the deep ocean, *J. Geophys. Res.*, 96(C2), 2723–2736.
- Webb, S. C. (1998), Broadband seismology and noise under the ocean, *Rev. Geophys.*, 36(1), 105–142.
- Wessel, P., and W. H. F. Smith (1991), Free software helps map and display data, *Eos Trans. AGU*, 72, 441–446.
- Wessel, P., W. H. F. Smith, R. Scharroo, J. F. Luis, and F. Wobbe (2013), Generic mapping tools: Improved version released, *Eos Trans. AGU*, 94(45), 409.
- Willoughby, E. C., K. Latychev, R. N. Edwards, K. Schwalenberg, and R. D. Hyndman (2008), Seafloor compliance imaging of marine gas hydrate deposits and cold vent structures, *J. Geophys. Res.*, 113, B07107, doi:10.1029/2005JB004136.
- Wolfe, C., S. Solomon, G. Laske, J. Collins, R. Detrick, J. Orcutt, D. Berovici, and E. Hauri (2009), Mantle shear-wave velocity structure beneath the Hawaiian hot spot, *Science*, 326, 1388–1390.
- Yang, Z., A. F. Sheehan, J. Collins, and G. Laske (2012), The character of seafloor ambient noise recorded offshore New Zealand: Results from the MOANA ocean bottom seismic experiment, *Geochem. Geophys. Geosyst.*, 13, Q10011, doi:10.1029/2012GC004201.
- Zha, Y., S. Webb, S. Nooner, and W. Crawford (2014), Spatial distribution and temporal evolution of crustal melt distribution beneath the East Pacific rise at 9°–10°N inferred from 3-D seafloor compliance modeling, *J. Geophys. Res.*, 119, 4517–4537, doi:10.1002/2014JB011131.